Internship Report

Bound state in graphene induced by atomic impurity

Tangchao Liu
M1 General Physics

tangchao.liu@universite-paris-saclay.fr

Laboratoire de Physique des Solides

June 2022

Abstract

The nearest neighbor hopping tight binding model on the honeycomb lattice of graphene gives rise to the relativistic desciption of electrons with a zero effective mass and linear dispersion relation, in low energy regime. If inversion symmetry is broken, the energy bands can open a gap. This work mainly studies the emergence of a single isolated state in this gap called bound state, which is induced by a local atomic impurity. Both analytic and numerical approach are adopted to compute the local density of state (LDOS) of gapless and gapped graphene, which is a direct expenrimental observable. Specifically, the far field behavior of LDOS is predicted by the Green function method in the continuum limit. It demonstrates an exponential decay inside the gap and Friedel oscillation pattern in the band, as well as the additional wavefront dislocations induced by the impurity. The emergence of bound state, the near impurity behavior of LDOS are shown by the tight binding numerical calculation. The wavefront dislocation for gapless graphene and spatial decaying behavoir for gapped graphene are recovered. A sharp peak right at the bound state energy does appear for DOS near the impurity at several fixed sites as a function of energy. A connection and agreement between the continuum analytic and discrete numeric approach is also built by computing the bound state position dependence on the impurity strength.

Contents

1 Introduction

A new era was opened for condensed matter physics since 1980s, with the introduction of the concept of topology and topological order into the field. The discovery of quantum Hall effect[1, 2] shaked the foundation of the two cornerstones of condensed matter theory[3], the Landau Fermi liquid theory and Landau's symmetry breaking formalism. Topology has played a key role to explain the robustness of this new kind of order for matter[4]. The geometrical phase induced by adiabatic evolution discovered by Berry[5] can be used to establish connections between the wavefunction and topology.

As the experimental technique and theoretical development continue to advance, the band structure topology of Dirac material has gained increasing attention over the decades. For the most celebrated Dirac material, graphene, the linear dispersion relation and pseudospin degrees of freeddom from two inequivalent sublattices has been revealed by scanning tunnelling microscope (STM) experiment[6]. In addition to the adiabatic cycle in the presence of magnetic field demonstrated by anomalous quantum Hall effect[7], the wavefront dislocations in Friedel oscillation induced by an atomic impurity also serves as a complementary approach to measure the quantized π-Berry phase from pseudospin winding[8]. Moreover, for graphene with inversion symmetry breaking, the bands open a gap and such atomic impurity can generate an isolated bound state in the band gap. Probing the properties of this bound state will give further information about the electronic band structure, which is not only interesting in view of theoretical understanding but is also the prerequisite for the potential application in technologies. This is what the present work is devoted to.

This report is organized as follows. Section 1 uses second quantization language to describe nearest neighbor tight binding model of graphene, with a focus on low energy regime. It also presents the Green function method used to calculate the local density of state (LDOS), an experimental observable. In section 3, the results of analytic calculations in the continuum limit is presented, demonstrating the Friedel oscillations and exponential decay for gapless and gapped graphene in the band gap respectively. Section 4 presents the results from tight binding numerical computations, including a reconstruction of wavefront dislocations for gapless graphene, the emergence of bound state for gapped graphene and its LDOS. Finally, section 5 summarizes the results and points out future work that can be done.

2 Theoretical preliminary

2.1 Tight binding on a honeycomb lattice

The honeycomb lattice has a primitive cell containing two carbon atoms, which under translation of basis vectors $\boldsymbol{a}_1$, $\boldsymbol{a}_2$ can pave the whole 2D plane. These two atoms, labelled by A and B, form two inequivalent sublattices on the plane under translation. The electrons on each A site can hop to 3 nearest B site, and vice versa for electrons

on each B site. A schematic sketch is shown in Fig 1. Therefore, the tight binding Hamiltonian in position space can be written as

$$H = t \sum_{\boldsymbol{r}_A} \sum_{\alpha=1}^{3} c_B^\dagger(\boldsymbol{r}_A + \boldsymbol{\delta}_\alpha) c_A(\boldsymbol{r_A}) + \text{h.c.}. \tag{2.1}$$

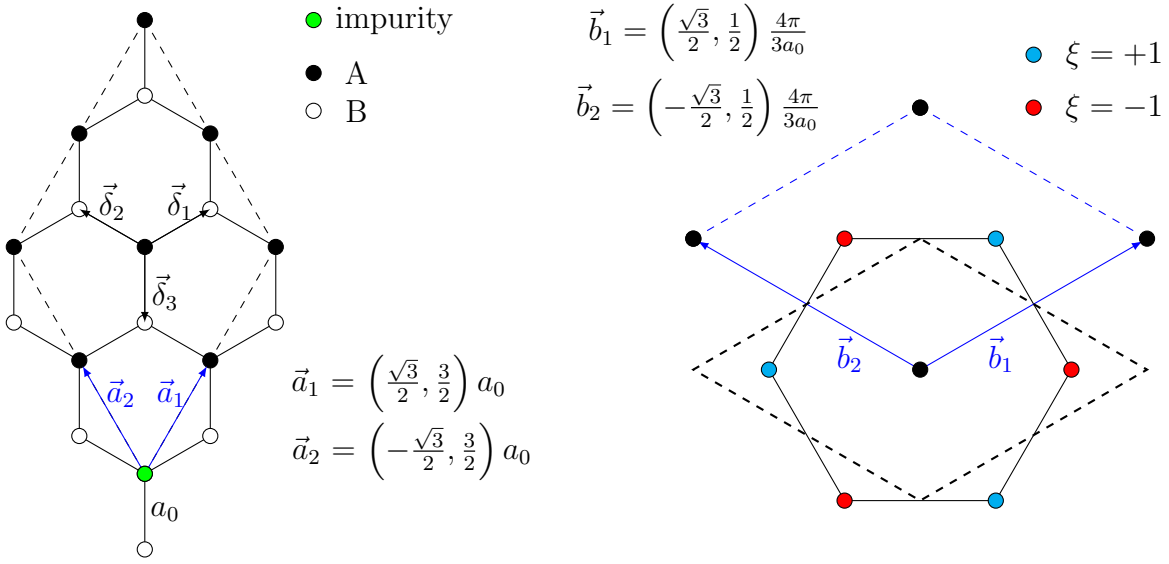

(a) Real lattice (b) Reciprocal lattice

Figure 1: A schematic sketch of the graphene lattices. (a) shows the real lattice with a size $N = 3$ on both directions of basis vectors $\boldsymbol{a}_1$ and $\boldsymbol{a}_2$. In numerical simulation the size N is much larger than 3 and periodic boundary condition is applied. This means the diamond shaped by the dashed line forms a torus. The lattice constant is roughly $a_0 \approx 1.42$Å. Electron at each A site can hop to three nearest B site separated by $\boldsymbol{\delta}_i$, $i = 1, 2, 3$ and vice versa. Throughout the work an atomic impurity is introduced at one A site chosen as the origin. (b) shows the reciprocal lattice, with $\boldsymbol{b}_1$ and $\boldsymbol{b}_2$ as the reciprocal basis vectors. Three choices of first Brillouin zone (BZ) are shown by hexagon, blue diamond and black diamond. The solid line Wigner-Seitz cell is conventional and its vertices are the valleys. In numerical calculations, the data are sampled in the blue diamond corresponding to the torus in (a). Sometimes the black dashed diamond is more convenient for calculation. The 3 choices are all equivalent up to a shift ot $\boldsymbol{b}_1$ and $\boldsymbol{b}_2$ of some parts of them.

For a graphene monolayer, the lattice constant and the hopping amplitude are roughly $a_0 \approx 1.42$Å and $t \approx -3$ eV. Under a lattice Fourier transformation $c_a(\boldsymbol{r}_i) = \frac{1}{\sqrt{N}} \sum_{\boldsymbol{k}} e^{i\boldsymbol{k}\cdot\boldsymbol{r}_i} c_a(\boldsymbol{k})$, where a labels the sublattice A or B, (2.1) can be written as

$$H/t = \sum_{\boldsymbol{k}} \sum_{a,b} c_a^\dagger(\boldsymbol{k}) \left[H(\boldsymbol{k})\right]_{ab} c_b(\boldsymbol{k}), \tag{2.2}$$

where the Hamiltonian matrix for one momentum value takes the 2×2 form, with the dimension 2 arising from sublattice d.o.f,

$$H(\boldsymbol{k}) = \begin{pmatrix} 0 & \sum_{\alpha=1}^{3} e^{i\boldsymbol{k}\cdot\boldsymbol{\delta}_\alpha} \\ \sum_{\alpha=1}^{3} e^{-i\boldsymbol{k}\cdot\boldsymbol{\delta}_\alpha} & 0 \end{pmatrix} = d_1(\boldsymbol{k})\sigma_1 + d_2(\boldsymbol{k})\sigma_2. \tag{2.3}$$

σ_1, σ_2 are the Pauli matrices. The Hamiltonian for a massive gapped graphene simply writes $H(\boldsymbol{k}) = d_1(\boldsymbol{k})\sigma_1 + d_2(\boldsymbol{k})\sigma_2 + M\sigma_3$. Physically it means the A and B sublattice are no longer the same type and inversion symmetry is broken. In real space, this mass term corresponds to an on-site energy M on the A site and $-M$ on the B site.

For gapless graphene it can be easily verified form (2.3) that at the momentum value

$$\boldsymbol{k} = \boldsymbol{K}^{\xi}_{mn} = \xi\frac{\boldsymbol{b}_1 - \boldsymbol{b}_2}{3} + m\boldsymbol{b}_1 + n\boldsymbol{b}_2, \qquad \xi = \pm 1, \quad m, n \in \mathbb{Z}, \tag{2.4}$$

the energy of the system $E(\boldsymbol{k}) = \pm\sqrt{d_1(\boldsymbol{k})^2 + d_2(\boldsymbol{k})^2}$ vanishes. These points are called the Dirac points and $\xi = \pm 1$ signifies two inequivalent valleys. Adiabatic transport around these valleys brings a π Berry phase, which is a smoking gun signature of band topology that has been verified[7, 8]. If in the momentum space, one focuses in the vicinity of the Dirac points and Taylor expand $H(\boldsymbol{K}^{\xi}_{mn} + \boldsymbol{q})$ in (2.3) up to linear order of $\boldsymbol{q}$

$$H(\boldsymbol{K}^{\xi}_{mn} + \boldsymbol{q}) = \begin{pmatrix} 0 & \xi q v_F e^{i\xi\theta_{\boldsymbol{q}}} \\ \xi q v_F e^{-i\xi\theta_{\boldsymbol{q}}} & 0 \end{pmatrix}, \tag{2.5}$$

with the Fermi velocity defined as $v_F = \frac{3}{2}a_0 t$, and the linear dispersion relation $E_{\pm}(\boldsymbol{K}^{\xi}_{mn} + \boldsymbol{q}) = \pm v_F q$. As is shown in Fig 1b, the first BZ only contains 1 pair of valleys. In the subsequent discussion it suffices to consider the pair enclosed by the black dashed line BZ, with m, n indices in (2.4) as $0, 0$. The $m, n = (0, 0)$ indices for the valleys are omitted from now on.

2.2 Green function and T-matrix formalism

The T-matrix formalism is widely used to calculate the analytic expression of LDOS in the presence of impurity[9, 10, 11]. For a system governed by Hamiltonian H_0, the starting point is the retarded Green function in energy domain $\hat{G}^{(0)}(\omega) = 1/(\omega + i0^+ - H_0)$, which comes from the forward propagation amplitude in time domain. The infinitesimal imaginary part added to energy ω comes from causality and emphasizes the *forward* propagation. It turns out that the imaginary part of diagonal element of $\hat{G}^{(0)}(\omega)$ in a certain resprentation $\{|\alpha_1\rangle, |\alpha_2\rangle, \dots\}$ actually signifies the intrinsic probability amplitude for the system to be in state $|\alpha_i\rangle$ and energy range $(\omega, \omega + \mathrm{d}\omega)$, apart from a factor of π^{-1}. In particular, if the chosen representation is position representation, the corresponding quantity is defined as the LDOS

$$\rho(\boldsymbol{r}; \omega) = -\frac{1}{\pi}\mathrm{Im}\left[G^{(0)}(\boldsymbol{r}, \boldsymbol{r}; \omega)\right]. \tag{2.6}$$

For a perturbed system with Hamiltonian $H = H_0 + V$, the Green function is expressed in the form of Dyson equation $G(\omega) = G^{(0)}(\omega) + G^{(0)}(\omega)VG(\omega)$ (for simplicity, the hat for abstract Green function before choosing any representation is omitted from now on). The intricacy of the Dyson series can be encoded in the so-called T-matrix denoted as $T(\omega)$

$$G(\omega) = G^{(0)}(\omega) + G^{(0)}(\omega)T(\omega)G^{(0)}(\omega), \qquad T(\omega) = V + VG^{(0)}(\omega)T(\omega), \tag{2.7}$$

where the solution to the T-matrixis simply writes $T(\omega) = V\left[1 - G^{(0)}(\omega)V\right]^{-1}$. And in this case, one is usually interested in calculating the LDOS modulation defined as

$$\delta\rho(\boldsymbol{r};\omega) = -\frac{1}{\pi}\mathrm{Im}\left[\langle\boldsymbol{r}|\, G^{(0)}(\omega)T(\omega)G^{(0)}(\omega)\,|\boldsymbol{r}\rangle\right]. \tag{2.8}$$

In the case of point impurity to be analyzed below, V is modeled by delta function, either Dirac delta in continuum case or Kronecker delta in discrete case.

3 Analytic calculations in the continuum limit

For a point impurity located on the A site chosen as coordinate origin, the matrix element of potential V is $\langle a, \boldsymbol{r}_1|\, V\,|b, \boldsymbol{r}_2\rangle = V_0\delta_{\boldsymbol{r}_1,\boldsymbol{r}_2}\delta_{\boldsymbol{r}_1,\boldsymbol{0}}\delta_{ab}\delta_{aA}$. The indices a, b stand for sublattice degrees of freedom. In the monolayer graphene, the system possesses translational invariance. Eventually the LDOS modulation can be written as

$$\begin{aligned}\delta\rho(\boldsymbol{r},\omega) &= -\frac{1}{\pi}\sum_{a=A}^{B}\mathrm{Im}\left[\langle a,\boldsymbol{r}|\, G^{(0)}(\omega)T(\omega)G^{(0)}(\omega)\,|a,\boldsymbol{r}\rangle\right] \\ &= \sum_{a=A}^{B} -\frac{1}{\pi}\mathrm{Im}\left[\frac{G^{(0)}_{aA}(\boldsymbol{r},\boldsymbol{0};\omega)V_0'G^{(0)}_{Aa}(-\boldsymbol{r},\boldsymbol{0};\omega)}{1 - G^{(0)}_{AA}(\boldsymbol{0},\boldsymbol{0};\omega)V_0'}\right].\end{aligned} \tag{3.1}$$

V_0' is the impurity strength in the continuum limit and has the unit [energy] $\cdot$ [length]^2. Because of translational invariance, the Green function matrix is diagonal in momentum representation (although not diagonal in sublattice degrees of freedom). Hence, in the continuum limit, the real space Green function can be obtained by the Fourier transform integral. First analyze gapless graphene without the mass term,

$$\begin{aligned}G^{(0)}(\boldsymbol{r},\boldsymbol{0};\omega) &= \int_{\boldsymbol{k}}\frac{\mathrm{d}k^2}{(2\pi)^2}e^{i\boldsymbol{k}\cdot\boldsymbol{r}}\left[\omega - H_0(\boldsymbol{k})\right]^{-1} \\ &= \sum_{\xi}e^{i\boldsymbol{K}^{\xi}\cdot\boldsymbol{r}}\int_{\mathbb{R}^2}\frac{\mathrm{d}q^2}{(2\pi)^2}\frac{e^{i\boldsymbol{q}\cdot\boldsymbol{r}}}{\omega^2 - (v_Fq)^2}\begin{pmatrix}\omega & \xi q v_F e^{i\xi\theta_{\boldsymbol{q}}} \\ \xi q v_F e^{-i\xi\theta_{\boldsymbol{q}}} & \omega\end{pmatrix}.\end{aligned} \tag{3.2}$$

The form in (2.5) is used. And the approximation of integrating over the whole 2D plane is assured by the suppresing factor $1/(\omega^2 - v_F^2q^2)$. Technically, the integral is contributed by the two poles on the real axis. This will change for the massive gapped graphene. The technical details are relagated to Appendix A. The result of the integral gives the Green function as

$$G^{(0)}(\boldsymbol{r},\boldsymbol{0};\omega) = -\frac{\omega}{(2v_F)^2}\sum_{\xi}e^{i\boldsymbol{K}^{\xi}\cdot\boldsymbol{r}}\begin{pmatrix} iH_0^{(1)}\left(\frac{\omega r}{v_F}\right) & \xi e^{i\xi\theta_{\boldsymbol{r}}}H_1^{(1)}(\frac{\omega r}{v_F}) \\ \xi e^{-i\xi\theta_{\boldsymbol{r}}}H_1^{(1)}(\frac{\omega r}{v_F}) & iH_0^{(1)}\left(\frac{\omega r}{v_F}\right)\end{pmatrix}, \tag{3.3}$$

where $H_0^{(1)}(x)$, $H_1^{(1)}(x)$ are zero and first order Hankel function of the first kind. The LDOS modulation, considering all the possible scattering among the valleys, is thus

obtained from (3.1) as[8]

$$\delta\rho(\boldsymbol{r};\omega) = \sum_{\xi,\xi'} C\ \mathrm{Im}\left[\omega^2 t(\omega)\left(H_0^{(1)}(\omega r/v_F)\right)^2\right]\cos(\Delta\boldsymbol{K}\cdot\boldsymbol{r}) \\ - C\ \mathrm{Im}\left[\omega^2 t(\omega)\left(H_1^{(1)}(\omega r/v_F)\right)^2\right]\xi\xi'\cos(\Delta\boldsymbol{K}\cdot\boldsymbol{r} - \Delta\xi\theta_{\boldsymbol{r}}), \tag{3.4}$$

where C is a constant independent of energy and position. $t(\omega) = V_0'/(1-G_{AA}^{(0)}(\mathbf{0},\mathbf{0};\omega)V_0')$. $\Delta\boldsymbol{K} = \boldsymbol{K}' - \boldsymbol{K}$. The oscillation pattern appearing here is dubbed Friedel oscillation.

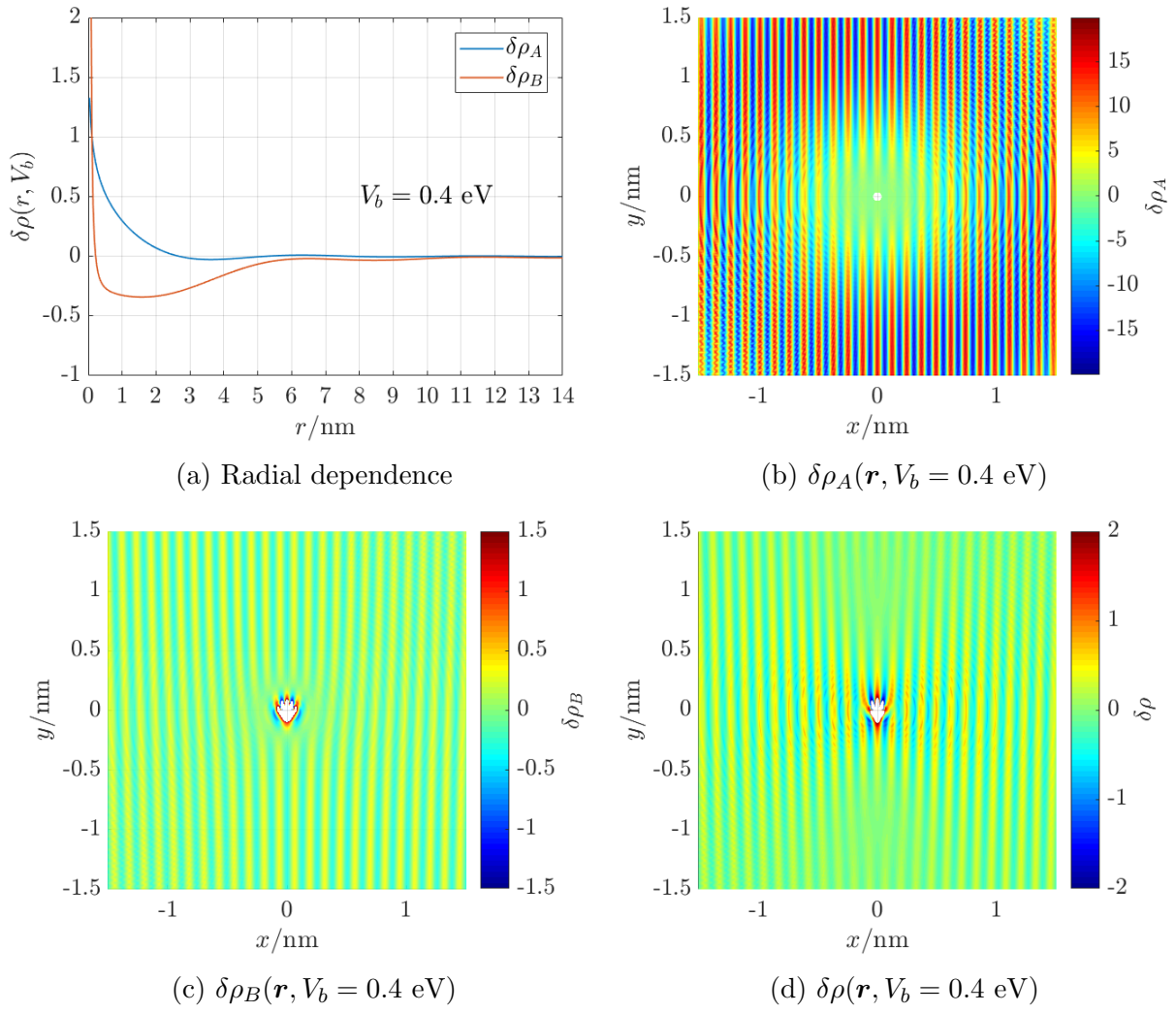

(a) Radial dependence

(b) $\delta\rho_A(\boldsymbol{r}, V_b = 0.4\text{ eV})$

(c) $\delta\rho_B(\boldsymbol{r}, V_b = 0.4\text{ eV})$

(d) $\delta\rho(\boldsymbol{r}, V_b = 0.4\text{ eV})$

Figure 2: LDOS in Eq.(3.4) for one pair of inter-valley scattering. The impurity strength chosen to generate the data is $V_0 = 1545t$. (a) shows the radial dependence of the prefactors before the cosines, achieved by integrating the expressions over ω up to the bias voltage of the STM tip $V_b = 0.4$ eV. This choice of bias voltage corresponds to [8]. It's rescaled with respect to $\delta\rho(r = 0.14\text{ nm})$. (b) shows $\delta\rho_A(\boldsymbol{r}, V_b = 0.4\text{ eV})$. The data in (b) is multiplied by r^2 to enhance visibility. There is no wavefront dislocation. (c) shows $\delta\rho_B(\boldsymbol{r}, V_b = 0.4\text{ eV})$. There are exactly 2 wavefront dislocations sourced by the vortex field in the phase. (d) displays the total LDOS from the two sublattices. The wavefront dislocations are less obvious but still tractable if examined very carefully.

At large distance it displays a dominant $1/r$ decay for monolayer graphene, due to the asymptotic behavior of the Hankel functions at $r \to \infty$

$$\left[H_0^{(1)}\left(\frac{\omega r}{v_F}\right)\right]^2 \simeq e^{\frac{2ir\omega}{v_F}-\frac{i\pi}{2}}\left(\frac{2v_F}{\pi r\omega}-\frac{iv_F^2}{2\pi r^2\omega^2}-\frac{5v_F^3}{16\pi r^3\omega^3}+O\left(\frac{1}{r^4}\right)\right) \tag{3.5}$$

$$\left[H_1^{(1)}\left(\frac{\omega r}{v_F}\right)\right]^2 \simeq e^{\frac{2ir\omega}{v_F}-\frac{3i\pi}{2}}\left(\frac{2v_F}{\pi r\omega}+\frac{3iv_F^2}{2\pi r^2\omega^2}+\frac{3v_F^3}{16\pi r^3\omega^3}+O\left(\frac{1}{r^4}\right)\right). \tag{3.6}$$

Treat $\delta\rho(\boldsymbol{r};\omega)$ as a wave field, the phase of the second term in (3.4) admits a contribution from a vortex field for inter-valley scattering $\Delta\xi = 2$, which sources the wavefront dislocations[12]. These wavefront dislocation are also experimentally verified[8]. A plot of this pattern for one pair of inter-valley scattering event from the analytical expression (3.4) is shown in Fig 2.

For the massive gapped graphene, the Hamiltonian $H(\boldsymbol{k})$ differs from (2.3) from M, $-M$ on the diagonal. The dispersion relation becomes $E(\boldsymbol{k}) = \pm\sqrt{d_1(\boldsymbol{k})^2 + d_2(\boldsymbol{k})^2 + M^2}$. Repeat the same procedure as above to compute the Green function in real space $G^{(0)}(\boldsymbol{r}, \boldsymbol{0}; \omega)$ and the LDOS modulation. In the energy range $|\omega| > M$, the Friedel oscillation pattern doesn't change essentially. What's interesting is to look in the band gap $-M < \omega < M$, where the integral in (3.2) only has contribution coming from the poles on the imaginary axis. Again, technical details can be found in Appendix A. The result is

$$G^{(0)}(\boldsymbol{r}, \boldsymbol{0}; \omega) = \sum_\xi \frac{e^{i\boldsymbol{K}^\xi\cdot\boldsymbol{r}}}{2\pi v_F^2}\begin{pmatrix} -(\omega+M)K_0(\frac{\Omega r}{v_F}) & -i\xi\Omega e^{i\xi\theta_{\boldsymbol{r}}}K_1(\frac{\Omega r}{v_F}) \\ -i\xi\Omega e^{-i\xi\theta_{\boldsymbol{r}}}K_1(\frac{\Omega r}{v_F}) & -(\omega-M)K_0(\frac{\Omega r}{v_F}) \end{pmatrix}, \tag{3.7}$$

where $\Omega = \sqrt{M^2-\omega^2} \in (0, M)$. $K_0(x)$ and $K_1(x)$ are the zero and first order modified Bessel function of the second kind. It's purely real for real argument and admits asymptotic behavior at $r \to \infty$

$$K_0\left(\frac{\Omega r}{v_F}\right) \simeq e^{-\frac{r\Omega}{v_F}}\left(\frac{\sqrt{\frac{\pi}{2}}\sqrt{\frac{v_F}{\Omega}}}{\sqrt{r}}-\frac{\sqrt{\frac{\pi}{2}}\left(\frac{v_F}{\Omega}\right)^{3/2}}{8r^{3/2}}+\frac{9\sqrt{\frac{\pi}{2}}\left(\frac{v_F}{\Omega}\right)^{5/2}}{128r^{5/2}}+O\left(1/r^{\frac{7}{2}}\right)\right) \tag{3.8}$$

$$K_1\left(\frac{\Omega r}{v_F}\right) \simeq e^{-\frac{r\Omega}{v_F}}\left(\frac{\sqrt{\frac{\pi}{2}}\sqrt{\frac{v_F}{\Omega}}}{\sqrt{r}}+\frac{3\sqrt{\frac{\pi}{2}}\left(\frac{v_F}{\Omega}\right)^{3/2}}{8r^{3/2}}-\frac{15\sqrt{\frac{\pi}{2}}\left(\frac{v_F}{\Omega}\right)^{5/2}}{128r^{5/2}}+O\left(1/r^{\frac{7}{2}}\right)\right). \tag{3.9}$$

Around the middle of the gap $\omega \approx 0$, the characteristic declay length is $v_F/2\Omega \sim (3/4)a_0 t/M$.

When applying (3.7) to (3.1), one has to substitute ω with $\omega + i\eta$ and first treat the Green function as if it's complex, then taking limit $\eta \to 0^+$ gives LDOS modulation

$$\delta\rho(\boldsymbol{r},\omega) = \sum_{a=A}^{B}\frac{1}{\pi}\frac{V_0'\mathrm{Re}\left[G_{aA}^{(0)}(\boldsymbol{r},\boldsymbol{0};\omega)G_{Aa}^{(0)}(-\boldsymbol{r},\boldsymbol{0};\omega)\right]\mathrm{Im}\left[-V_0'G_{AA}^{(0)}(\boldsymbol{r},\boldsymbol{0};\omega)\right]}{\left[1-V_0'\mathrm{Re}\left(G_{AA}^{(0)}(\boldsymbol{0},\boldsymbol{0};\omega)\right)\right]^2+\left[\mathrm{Im}\left(-V_0'G_{AA}^{(0)}(\boldsymbol{r},\boldsymbol{0};\omega)\right)\right]^2}. \tag{3.10}$$

The whole expression gives 0 unless both numerator and denominator vanish, since in the band gap the Green function is purely real. Making use of the property of of Dirac

delta function $\lim_{\gamma\to 0}\frac{1}{\pi}\frac{\gamma}{E(\omega)^2+\gamma^2} = \delta(E(\omega)) = \frac{\delta(\omega-\omega_b)}{|E'(\omega_b)|}$ in (3.10), where ω_b is the solution simultaneously satisfying

$$\mathrm{Im}\left[-V_0' G^{(0)}_{AA}(\boldsymbol{r},\boldsymbol{0};\omega)\right] = 0, \qquad E(\omega) \equiv 1 - V_0' \mathrm{Re}\left(G^{(0)}_{AA}(\boldsymbol{0},\boldsymbol{0};\omega)\right) = 0. \tag{3.11}$$

Then the LDOS modulation gives

$$\delta\rho(\boldsymbol{r},\omega) = \sum_{a=A}^{B} \mathrm{Re}\left[G^{(0)}_{aA}(\boldsymbol{r},\boldsymbol{0};\omega) G^{(0)}_{Aa}(-\boldsymbol{r},\boldsymbol{0};\omega)\right] \frac{\delta(\omega-\omega_b)}{|E'(\omega_b)|}. \tag{3.12}$$

A single isolated state with energy ω_b appears in the gap due to the presence of the impurity. This is the so-called bound state. The spatial pattern of the local density of state for such a bound state is highly localized around the impurity, as is evidenced by the asymptotic behavior of exponential decay at large distance.

The continuum analytic calculation predicts the existence of bound state. However, it fails to predict the position of the bound state in the gap. When one tries to solve the second equation in (3.11),

$$1 - V_0' \mathrm{Re}\left[G^{(0)}_{11}(\boldsymbol{0},\boldsymbol{0};\omega)\right] = 1 + \frac{V_0' N_v(\omega+m)}{2\pi v_F^2} K_0(0) = 0. \tag{3.13}$$

N_v is the number of valleys involved. $K_0(x)$ diverges at $x = 0$ and renders the theory pathological. In fact, the continuum calculation cannot be trusted anymore when it gets too close to the origin, i.e., to the impurity, since there are still a finite distance from the impurity to its neighbor carbon atom at the order of $a_0 \sim 1.42$Å. Heuristically, a cut-off at the lattice scale approximately at $r \approx a_0$ can be introduced to (3.13), taking into account the definition of Fermi velocity $v_F = \frac{3}{2}a_0 t$ and the number of valleys $N_v = 2$,

$$\frac{V_0'/(\beta a_0^2)}{t}\left(\frac{\omega_b}{t}+\frac{M}{t}\right) K_0\left(\frac{2}{3}\sqrt{\left(\frac{M}{t}\right)^2 - \left(\frac{\omega_b}{t}\right)^2}\right) = -\frac{9\pi}{4}. \tag{3.14}$$

$V_0 = V_0'/(\beta a_0^2)$ is the impurity strength in discrete lattice and is referred to as impurity strength from now on. The argument of $K_0(\Omega r/v_F)$ is chosen exactly at $r = a_0$. The determination of numerical factor β will be illuminated in comparison with the data coming tight binding numerical computation.

4 Tight binding numerics

In this task, the periodic boundary condition is adopted on both $\boldsymbol{a}_1$ and $\boldsymbol{a}_2$ direction. The number of unit cells N chosen on both direction is the same $N = 102$, such that the sampling of lattice points in momentum space will go through the Dirac points. When the Hamiltonian is diagonalized as $H = \sum_\alpha \epsilon_\alpha d_\alpha^\dagger d_\alpha$, the eigenvectors $U_{j\alpha}$ appearing in the expression of these quasi-particle creation and annihilation operators

$$d_\alpha^\dagger = \sum_j \langle j|\alpha\rangle\, c_j^\dagger = \sum_j U_{j\alpha} c_j^\dagger \qquad d_\alpha = \sum_i \langle\alpha|i\rangle\, c_i = \sum_i U_{i\alpha}^* c_i \tag{4.1}$$

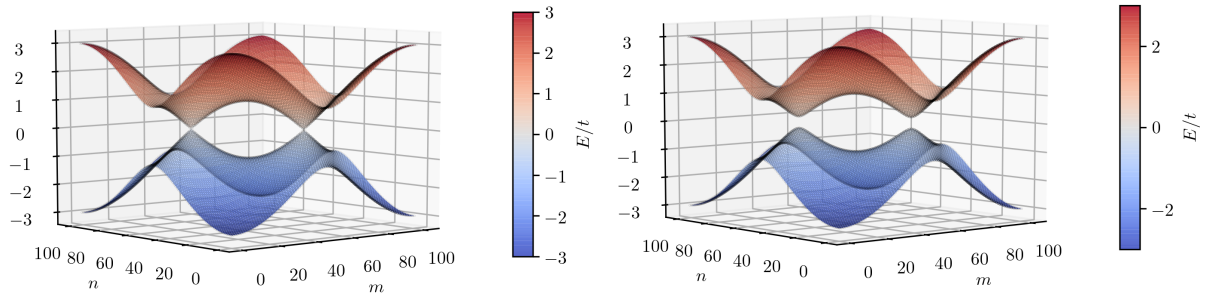

(a) Gapless bands

(b) Gapped bands

Figure 3: The energy bands for massless and massive electrons. The numerous black dots are the numerical solutions ϵ_α to the Hamiltonian in real space. They lie almost exactly on the bands plotted according to analytic solution. The bands are plotted as a function of the indices m, n for wavevector $\boldsymbol{k} = \frac{m}{N}\boldsymbol{b}_1 + \frac{n}{N}\boldsymbol{b}_2$.

are nothing but the position space wavefunctions for various energy eigenstates with eigenenergy ϵ_α. The Hamiltonian matrix is real and symmetric, so the software will automatically return real eigenvectors. This corresponds to a superposition of the plane wave eigenstate $e^{i\boldsymbol{k}\cdot\boldsymbol{r}}$ and $e^{-i\boldsymbol{k}\cdot\boldsymbol{r}}$ with the same eigenenergy ϵ_α such that the resulting wavefunctions are purely real in this energy subspace. The upshot is that the probability density $|U_{j\alpha}|^2$ and the LDOS for electrons in pristine graphene both exhibit a wavy behavior as a signature of standing wave, be it in the massless or massive regime. This is purely an artificial effect from numerical computation. According to Heisenberg uncertainty principle, the electron completely localized in momentum space, such as in this case, will be completely delocalized in the position space. The translational invariance suggests that no lattice site should be preferable than the others in the absence of impurity. So the strategy for computing the LDOS in numerical method is modified. One only computes the LDOS of the contaminated graphene, without subtracting the LDOS of pristine graphene which involves the artifact of standing wave behavior.

The numerical calculation of energy spectrums for massless and massive pristine graphene agree fairely well with the analytical result, as is shown in Fig 3. This serves as a validity check of the code to simulate the Hamiltonian.

4.1 Gapless graphene with impurity

The impurity is located only on one A site chosen as the origin and its strength is chosen as $V_0/t = 1545$. The simulated LDOS data $\rho(\boldsymbol{r};\omega)$ contains the pattern of oscillation coming from scattering among the valleys. The Fourier transform of the data $\rho(\boldsymbol{r};\omega)$ is obtained for both A and B sublattice, for the energy value $\omega = 0.13t$, which correspond to the choice in Fig 2 of Dutreix et, al[8]. The Fourier transformed LDOS in momentum space is plotted in Fig 4. One can see the dominant signals coming from inter and intra-valley scattering as they peak. Using Gaussian wavepacket to filter out only the inter-valley scattering, the reconstructed LDOS in real space by inverse Fourier transform are plotted in Fig 5. The two wavefront dislocations appear in the total charge oscillation.

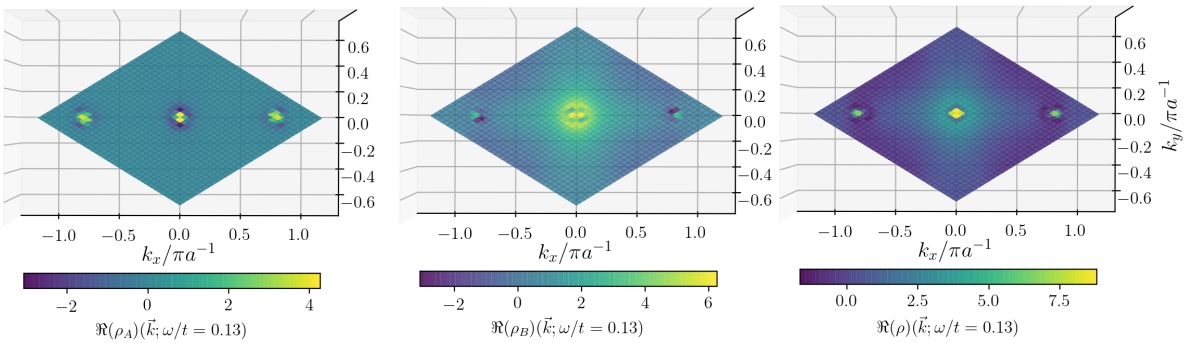

(a) $\mathrm{Re}(\rho_A(\boldsymbol{k}))$ (b) $\mathrm{Re}(\rho_B(\boldsymbol{k}))$ (c) $\mathrm{Re}(\rho(\boldsymbol{k}))$

Figure 4: LDOS for contaminated gapless graphene in momentum space, plotted as the black dashed line shaped diamond BZ in Fig 1b. By a suitable translation of $\boldsymbol{b}_1$ and $\boldsymbol{b}_2$ the diamond shaped first Brillouin zone can be made into traditional hexagon shape. The impurity strength is $V_0 = 1545t$. It's plotted for energy $\omega \approx 0.13t$. The peak in the center corresponds to intra-valley scattering. The peaks on the two valleys $\boldsymbol{K}^\xi = \xi(\boldsymbol{b}_1 - \boldsymbol{b}_2)/3$, $(\xi = \pm 1)$ correspond to inter-valley scattering. This pattern agrees with the results found in [10]. The filtering in momentum space is done by Gaussian wavepackets around the two peaks opposite to each other with respect to the origin, with a standard deviation $\sigma = b/8\sqrt{3}$, where $b = |\boldsymbol{b}_1| = |\boldsymbol{b}_2|$.

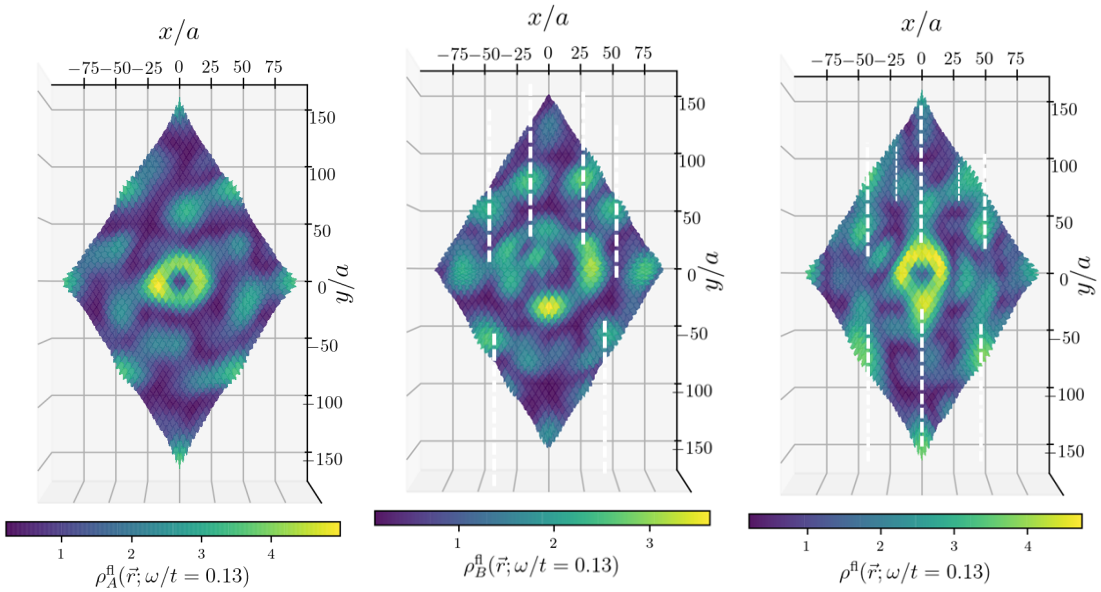

(a) $\rho_A(\boldsymbol{r})$ (b) $\rho_B(\boldsymbol{r})$ (c) $\rho(\boldsymbol{r})$

Figure 5: The filtered real space LDOS obtained from inverse Fourier transform for contaminated gapless graphene. The plots shown here are the norm of the data $\rho^{\mathrm{fl}}(\boldsymbol{r};\omega)$, with a small imaginary part arising from the finite width of Gaussian filtering wavepackets. In these plots, it's on average 3 to 4 orders of magnitude smaller than the real part, for the standard deviation chosen as $\sigma = b/8\sqrt{3}$. It can be made even smaller by decreasing this width σ. The data is multiplied by 10^4 for the convenience of colorbar display. Several wavefronts are labelled by white dashed line. The two dislocations appear in $\rho_B(\boldsymbol{r})$ and the total $\rho(\boldsymbol{r})$ but is less obvious in the latter.

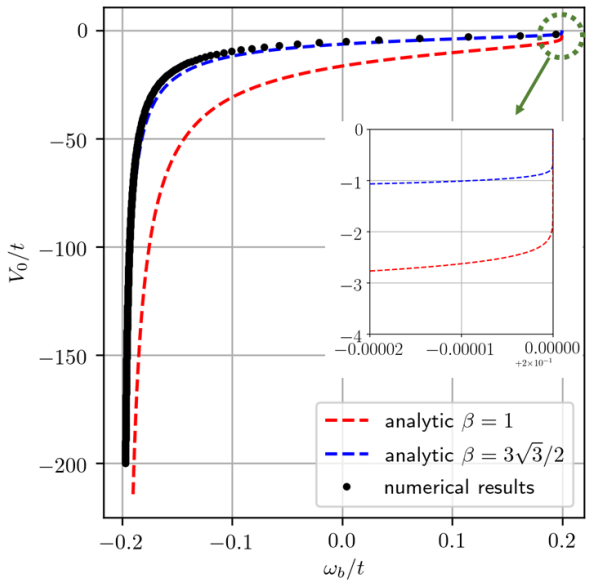

(a) Bound state position for $M = 0.2t$ and various V_0

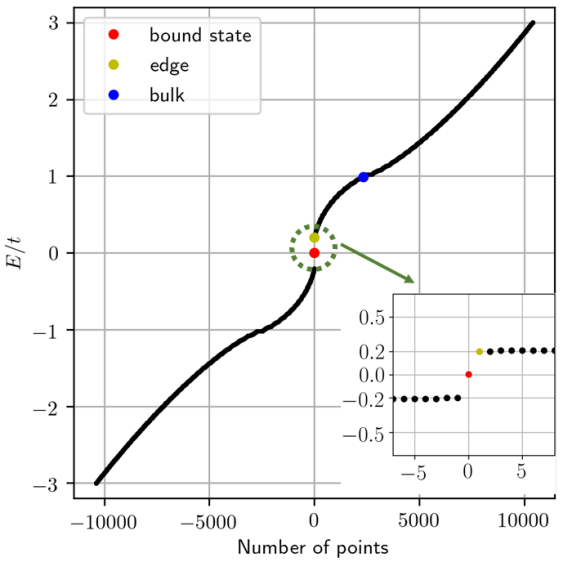

(b) Eigenenergies for $V_0 = -5t,\ M = 0.2t$

Figure 6: Bound state position for various impurity strength and eigenenergy distribution for $V_0 = -5t,\ M = -2t$. In (a), the dashed lines are plotted according to Eq.(3.14). The area of the primitive cell for graphene honeycomb lattice is exactly $\beta a_0^2 = (3\sqrt{3}/2)a_0^2$. This choice of β corresponds to the blue dashed line in (a) and is in agreement with the numerical data. A zoomed in view exhibits a threshold of impurity strength for the appearance of bound state. In (b), the eigenenergy $\epsilon_\alpha \approx V_0$ is excluded from the plot. The three colored points are selected to plot the spatial pattern of LDOS $\rho(\boldsymbol{r};\omega)$. The bound state is labelled by red. Its location near the center of the gap makes its property most pronounced, which will be shown by the sharp peaks in Fig 7 and Fig 8. As is shown in (a), a larger impurity strength brings the bound state closer to the lower band edge. The signal of bound state in DOS will also be less significant.

4.2 Gapped graphene with impurity

The analytic analysis predicts the existence of bound state in the band gap, but fails to predict its position, due to its failure near the impurity point. From numerical simulation with the choice of mass $M = 0.2t$, the bound state position in the gap for various impurity strength is calculated and plotted in Fig 6a. Remarkably, it's almost exactly predicted by the heuristic cut-off in analytic expression at $r = a_0$, provided that the area factor β in (3.14) is accounted for by the unit cell area. This builds a strong connection between analytic and numerical treatment. The eigenenergies solved for Hamiltonian with parameters $V_0 = -5t$, $M = 0.2t$ is plotted in Fig 6b. This choice of parameter is to make the bound state appear near the gap center so that the bound state signature is most pronounced.

The density of state at a few sites around the impurity $\rho_A(\omega)$ and $\rho_B(\omega)$ as a function of energy ω are displayed in Fig 7 and Fig 8.The sharp peak at the bound state is a signature of Dirac delta function in the analytic results. In addition, the spatial pattern

of real space LDOS for the three energies selected in Fig 6b is plotted in Fig 9 and Fig 10. The same Fourier analysis and filtering is done for LDOS at the bound state energy $\rho(\boldsymbol{r};\omega_b)$. This is shown in Fig 11 and Fig 12. The rapid decaying behavior over a few sites are again recovered. But no exponentially suppressed wavefront dislocation is displayed. It should result from the absence of inter-valley scattering for B sublattice in Fourier space shown in Fig 11b. This seems to be at odds with the analytic result (3.12). It suggests a limitation of the numerical calculations performed here, probably due to an improper choice of parameters or a limited lattice size.

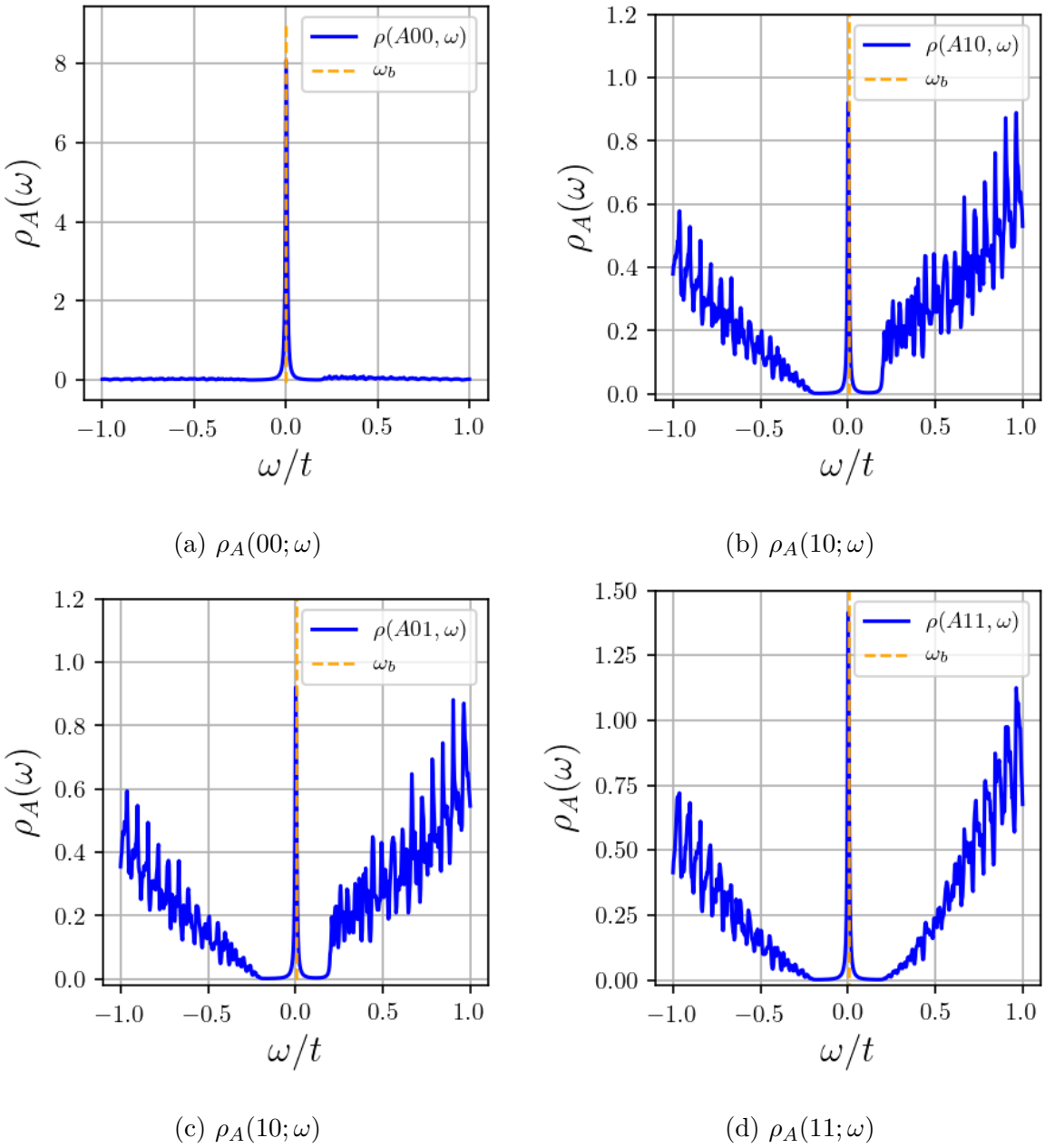

(a) $\rho_A(00;\omega)$

(b) $\rho_A(10;\omega)$

(c) $\rho_A(10;\omega)$

(d) $\rho_A(11;\omega)$

Figure 7: $\rho_A(\omega)$ for sites (00), (10), (01), (11) respectively. A very sharp peak arises right at the position of bound state labelled by red in Fig 6b, in the otherwise flat band gap. The sharp peak is a signature of the Dirac delta function in (3.12). This is another aspect of the agreement between analytic and numerical approach.

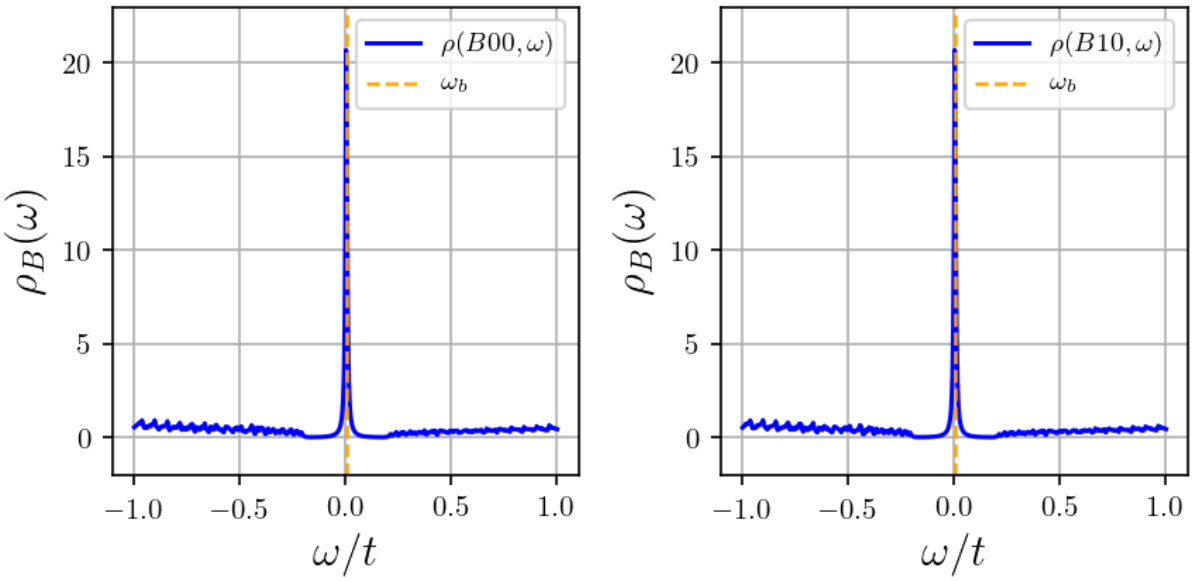

(a) $\rho_B(00;\omega)$

(b) $\rho_B(10;\omega)$

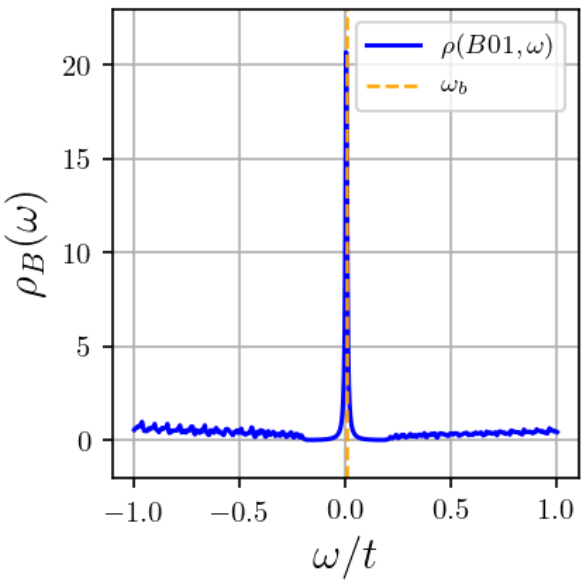

(c) $\rho_B(10;\omega)$

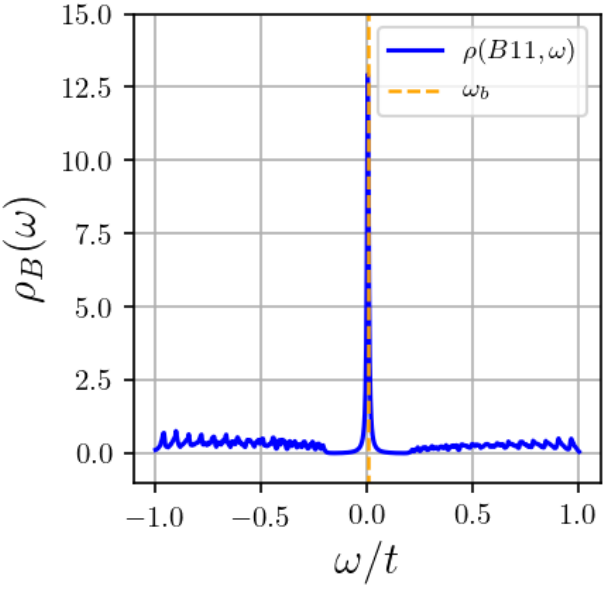

(d) $\rho_B(11;\omega)$

Figure 8: $\rho_B(\omega)$ for sites (00), (10), (01), (11) respectively. Again there's a sharp peak at the bound state, as a signature of Dirac delta function in analytic result (3.12). The energy dependence for B sublattice behaves the same for the sites near the A impurity. This again shows different response of LDOS to the impurity for A and B sublattice.

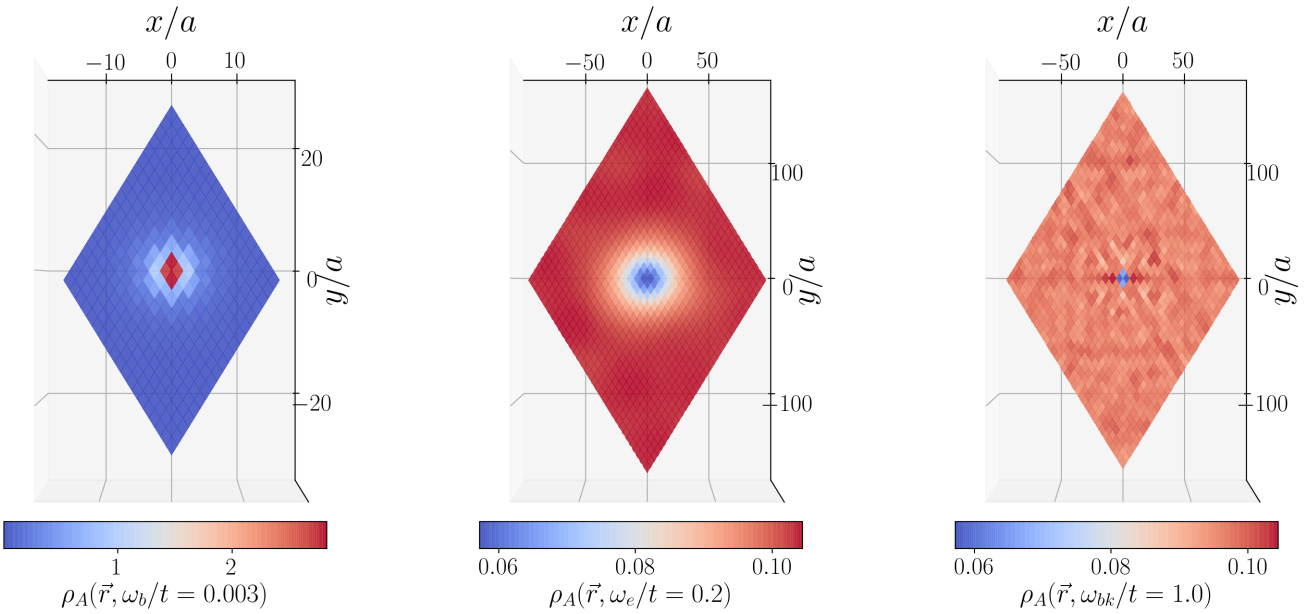

(a) $\rho_A(\boldsymbol{r};\omega)$ for ω at bound state, band edge and band bulk

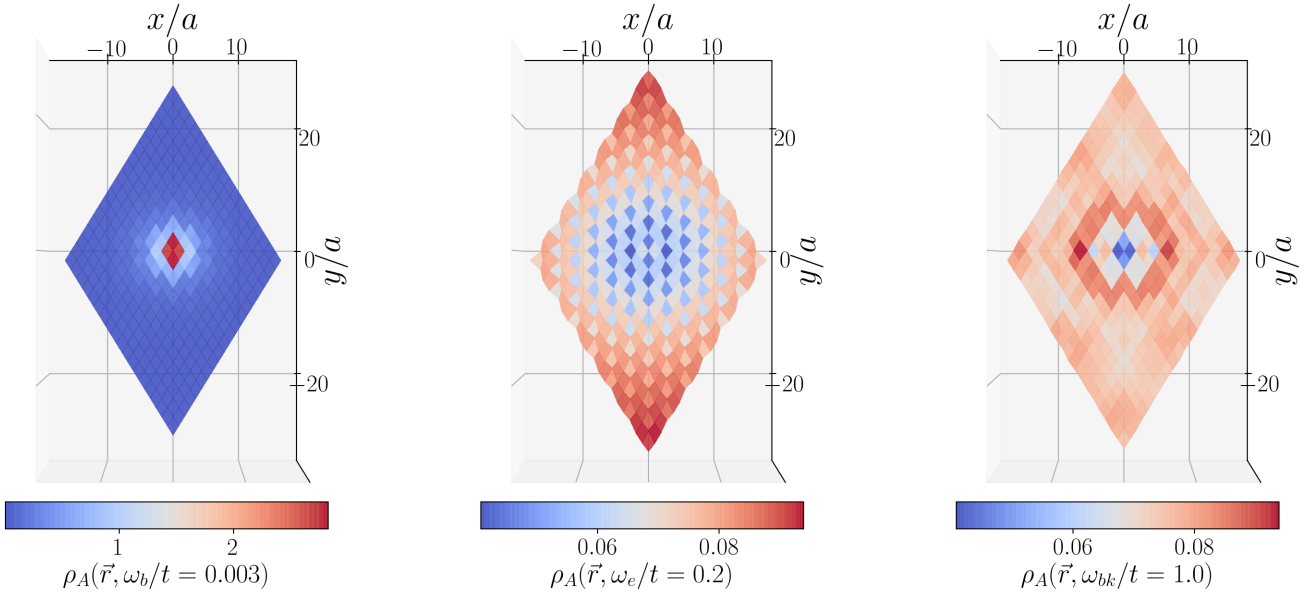

(b) Middle and right panel zoomed in

Figure 9: $\rho_A(\boldsymbol{r};\omega)$ for sublattice A at the three energy values. The origin is shifted to the center, compared to Fig 1a, due to periodicity. Only the bound state energy plot is not zoomed in. It decays to zero after just a few sites from the impurity. Such a rapid decaying behavior qualitatively agrees with the results in analytic method. The spatial pattern obeys symmetry of reflection about the direction $\boldsymbol{a}_1+\boldsymbol{a}_2$ and $\boldsymbol{a}_1-\boldsymbol{a}_2$, as it should be since the local impurity is located only on one A site located at the origin.

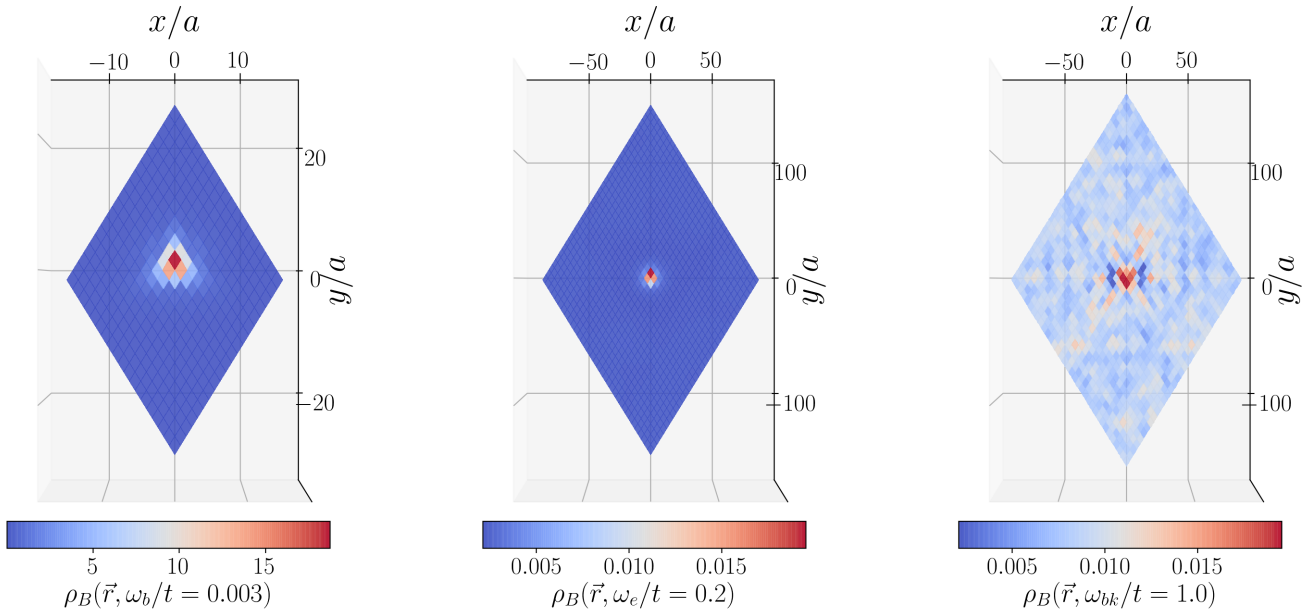

(a) $\rho_B(\boldsymbol{r};\omega)$ for ω at bound state, band edge and band bulk

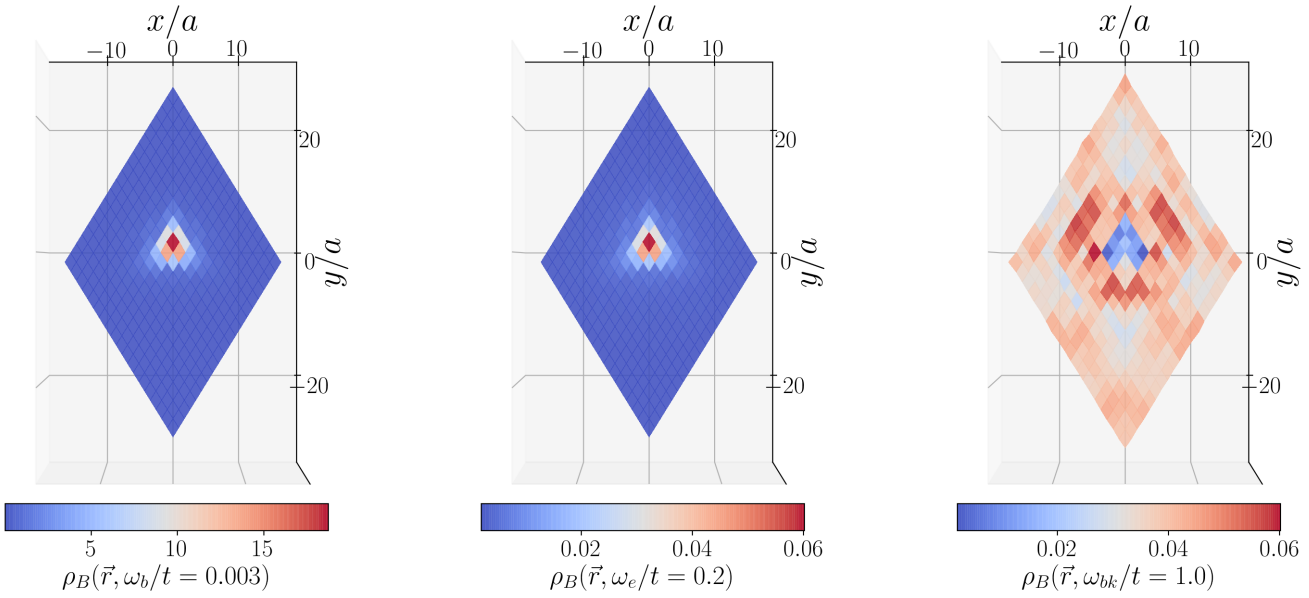

(b) Middle and right panel zoomed in

Figure 10: $\rho_B(\boldsymbol{r};\omega)$ for sublattice B at the three energy values. Again only the bound state energy is not zoomed in. The pattern for ω_b and ω_e are almost the same for B sublattice, except for the numerics. The B lattice LDOS responses to the impurity differently from that of A sublattice. It's only symmetric by reflection about the direction $\boldsymbol{a}_1 + \boldsymbol{a}_2$, which makes sense since the impurity lies right above the B atom at the $m, n = (00)$ site.

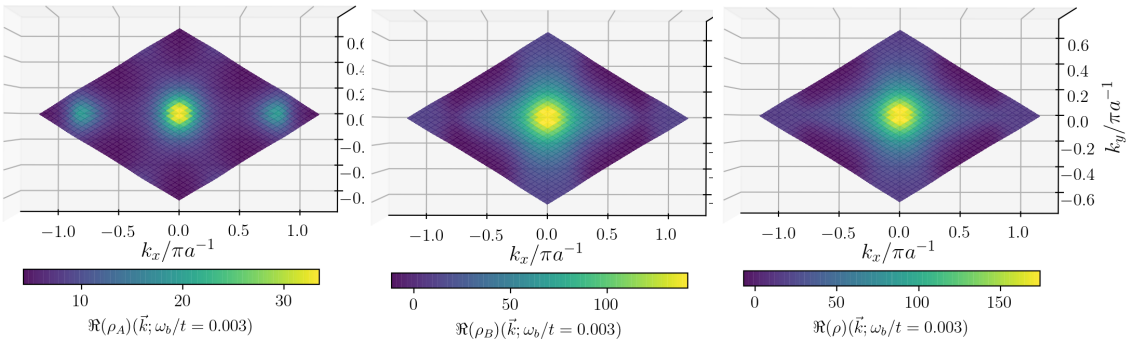

(a) $\mathrm{Re}(\rho_A(\boldsymbol{k}))$ (b) $\mathrm{Re}(\rho_B(\boldsymbol{k}))$ (c) $\mathrm{Re}(\rho(\boldsymbol{k}))$

Figure 11: The real part of Fourier tranform of the LDOS for bound state shown in left panels of Fig 9 and Fig 10. For A sublattice both intra and inter-valley scattering are present. But for B sublattice there is only intra-valley scattering. Superimposing the two gives only dominant signal for intra-valley scattering. Again, Gaussian wavepackets around the two valleys are used to filtered the signals around them. The width is chosen as $\sigma = b/16\sqrt{3}$. This leads to the results shown in Fig 12.

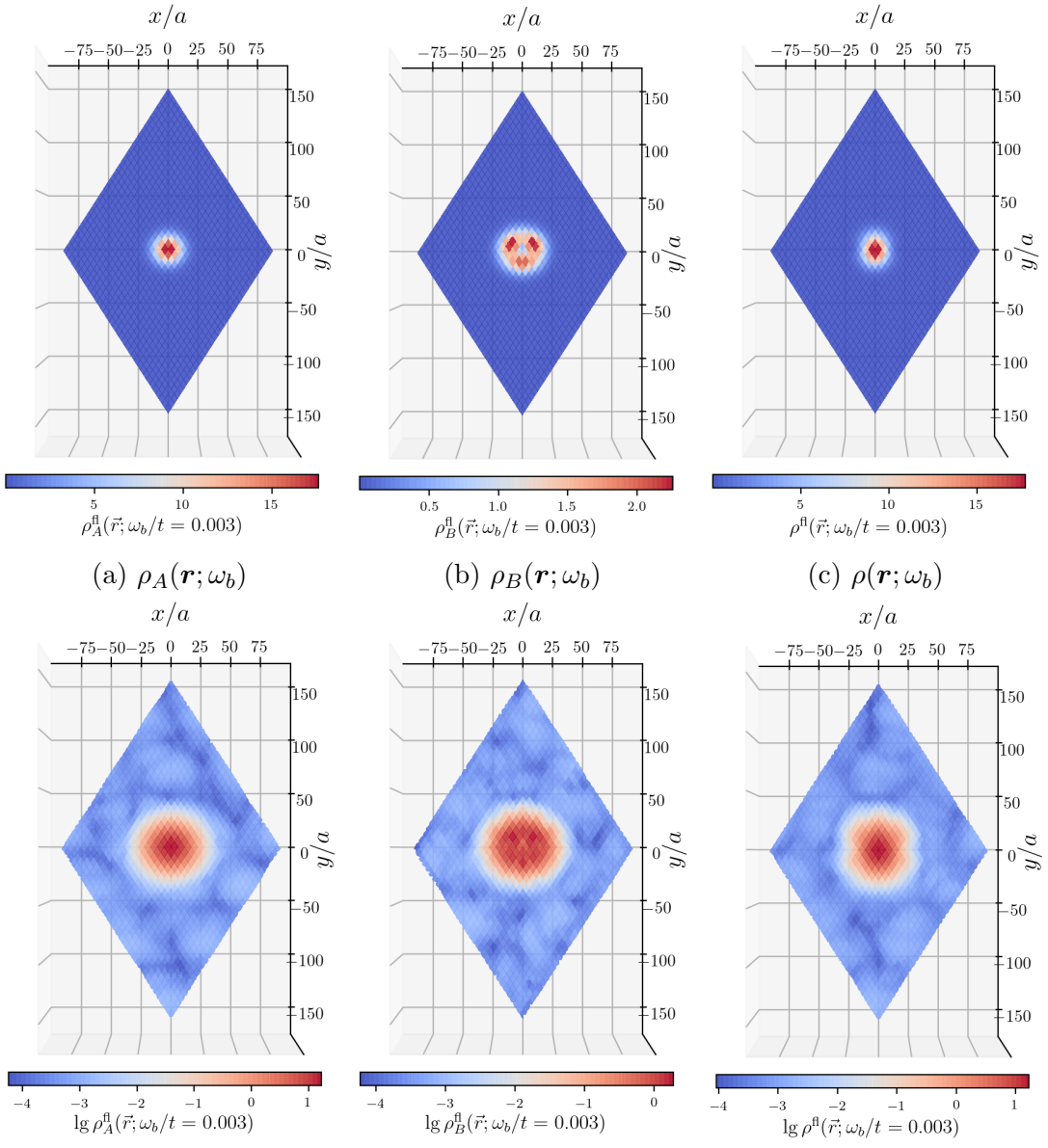

(a) $\rho_A(\boldsymbol{r};\omega_b)$ (b) $\rho_B(\boldsymbol{r};\omega_b)$ (c) $\rho(\boldsymbol{r};\omega_b)$

(d) $\lg\rho_A(\boldsymbol{r};\omega_b)$ (e) $\lg\rho_B(\boldsymbol{r};\omega_b)$ (f) $\lg\rho(\boldsymbol{r};\omega_b)$

Figure 12: The filtered bound state LDOS. The bottom three panels show the data in log scale. Most of the behavior of the left panels of Fig 9 and Fig 10 are recovered, including the rapid decay around the impurity, the reflection symmetry about certain axes for the two sublattices. The data $\rho(\boldsymbol{r};\omega)$ shown here are multiplied by a factor of 10^4 for the convenience of colorbar display. The absence of wavefront dislocation might be due to the absence of inter-valley scattering in Fig 11b.

5 Conclusion

In summary, the analytic and numerical method are both applied to study the gapless and gapped monolayer graphene, in particular the isolated bound state in the middle of the gap induced by an atomic impurity. Some agreements between these two approaches are established, demonstrating the efficiency of this dichotomy.

The main result is the calculation of LDOS, an experimental observable probed by STM. In analytic analysis, for gapless graphene the LDOS is shown to display Friedel oscillations and wavefront dislocations induced by the vortex field in the presence of impurity. The LDOS for the case of massive electrons on graphene exhibits an exponential decay inside the band gap, with a characteristic decay length $l_{\text{decay}} \sim a_0 t/M$. The analytic result in the continuum limit predicts the existence of the bound state inside the gap but fails to predict its position, because the real system is after all in the form of a discrete lattice. In tight binding numerical calculations, the spectra of the Hamiltonian for the two types of graphene are computed. In particular, the position of the bound state in the gap is calculated for a set of impurity strength, which considerably agrees with the cut-off in the analytic expression taking into account of the area factor of a unit cell in graphene honeycomb lattice. The eigenenergies and wavefunctions serve as the input to calculate the LDOS which mimic experimental data. This allows to build several other connections between analytics and numerics. For instance, for gapless graphene, the wavefront dislocations are vaguely reconstructed from Gaussian filtering of LDOS data in Fourier space. For gapped graphene, the rapid exponential decaying behavior of LDOS for bound state is recovered. The DOS as a funtion of energy ω exhibits a sharp peak right at the value of bound state energy, which is a signature of Dirac delta function in the analytical expression. Finally, the same Gaussian filtering technique is attempted to recover the exponentially suppressed wavefront dislocations for bound state. But within the numerical limitations of the tight binding computations performed here, we were unable to extract the signal of analytically predicted spatial modulations.

Improvement and generalization can be done. One can try to improve the resolution of wavefront in the filtered LDOS data, by trying to increase the size of lattice if computational power allows. The reason for the absence of inter-valley scattering and the wavefront dislocation for the bound state is yet to be examined. Once the work on graphene is completed, one can start to consider a magnetic point impurity on other types of 2D material, such as transition metal dichalcogenides (TMD), where electrons with different spins react differently to the impurity. How will the bound state be gen-

erated in such scenario? And what will be its difference from the case of non-magnetic impurity considered in this work? These questions can be explored in the future by both theoretical and experimental work.

A Calculation details for analytic Green function

This appendix presents some details about using some complex analysis to compute the analytic expression of real space Green functions. It's adapted from appendix B,C of [9]. For simplicity, the Fermi velocity is set to $v_F = 1$ during the calculations and restored in the final results.

Two integrals will be frequently used in the subsequent calculation.

$$I^{(1)}_{M,N}(\boldsymbol{r},\omega) = \int_{\mathbb{R}^2} \frac{\mathrm{d}q^2}{(2\pi)^2} \frac{q^{2M}}{\omega^2 - q^{2N}} e^{i\boldsymbol{q}\cdot\boldsymbol{r}}, \tag{A.1}$$

$$I^{(2)}_{L,M,N}(\boldsymbol{r},\omega) = -\int_{\mathbb{R}^2} \frac{\mathrm{d}q^2}{(2\pi)^2} \frac{q^{2M}}{\omega^2 - q^{2N}} \left(qe^{i\xi\theta_{\boldsymbol{q}}}\right)^L e^{i\boldsymbol{q}\cdot\boldsymbol{r}}. \tag{A.2}$$

For $I^{(1)}_{M,N}(\boldsymbol{r},\omega)$, making use of the integral definition of the integer order Bessel function $J_n(x)$ and the result

$$\int_1^\infty \frac{\mathrm{d}u}{\pi} \frac{\sin(qru)}{\sqrt{u^2-1}} = \frac{1}{2} J_0(qr), \tag{A.3}$$

$I^{(1)}_{M,N}(\boldsymbol{r},\omega)$ can be written as

$$\begin{aligned} I^{(1)}_{M,N}(\boldsymbol{r},\omega) &= \int_0^\infty \frac{\mathrm{d}q}{2\pi} \frac{q^{2M+1}}{\omega^2 - q^{2N}} J_0(qr) \\ &= \int_0^\infty \frac{\mathrm{d}q}{\pi} \frac{q^{2M+1}}{\omega^2 - q^{2N}} \int_1^\infty \frac{\mathrm{d}u}{\pi} \frac{\sin(qru)}{\sqrt{u^2-1}} \\ &= \frac{1}{2\pi^2} \int_1^{+\infty} \frac{\mathrm{d}u}{\sqrt{u^2-1}} \int_{-\infty}^{+\infty} \mathrm{d}q \frac{q^{2M+1}\sin(qru)}{\omega^2 - q^{2N}} \\ &= \frac{1}{2\pi^2} \int_1^{+\infty} \frac{\mathrm{d}u}{\sqrt{u^2-1}} \sum_{n=0}^{2N-1} \frac{1}{2N q_n^{2(N-M-1)}} \int_{\mathbb{R}} \mathrm{d}q \frac{\sin(qru)}{q_n - q}. \end{aligned} \tag{A.4}$$

$q_n = \omega^{1/N} e^{i\frac{n}{N}\pi}$ is the nth (n from 0 to $2N-1$) simple pole of the integrand over q, among the $2N$ simle poles. q_0 and q_N are the poles lying on the real axis. The distribution of poles is shown in Fig 13. For the monolayer graphene considered in this work, $N = 1$ suffices. The case of a generic positive integer N can be used to study the Green function of N-layer graphene[9].

For $I^{(2)}_{L,M,N}(\boldsymbol{r},\omega)$, a recursion relation with $I^{(1)}_{M,N}(\boldsymbol{r},\omega)$ can be built.

$$\begin{aligned} I^{(2)}_{L,M,N}(\boldsymbol{r},\omega) &= -\int_{\mathbb{R}^2} \frac{\mathrm{d}q^2}{(2\pi)^2} \frac{q^{2M}}{\omega^2 - q^{2N}} \left(qe^{i\xi\theta_{\boldsymbol{q}}}\right)^L e^{i\boldsymbol{q}\cdot\boldsymbol{r}} \\ &= -\int_0^\infty \frac{\mathrm{d}q}{2\pi} \frac{q^{2M+1}}{\omega^2 - q^{2N}} \frac{q^L e^{i\xi L\theta_{\boldsymbol{r}}}}{2\pi} \int_0^{2\pi} \mathrm{d}\theta_{\boldsymbol{q}} e^{i\xi L(\theta_{\boldsymbol{q}} - \theta_{\boldsymbol{r}})} e^{iqr\cos(\theta_{\boldsymbol{q}} - \theta_{\boldsymbol{r}})} \\ &= -\xi^L \int_0^\infty \frac{\mathrm{d}q}{2\pi} \frac{q^{2M+1}}{\omega^2 - q^{2N}} e^{i\xi L(\theta_{\boldsymbol{r}} + \frac{\pi}{2})} q^L J_L(qr), \end{aligned} \tag{A.5}$$

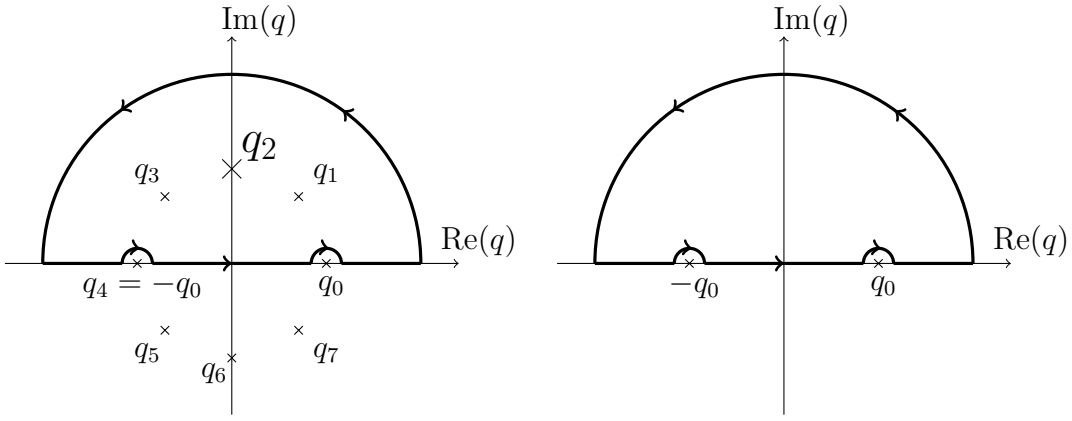

(a) q_n distribution for $N = 4$ (b) $N = 1$ for gapless graphene

Figure 13: Simple pole distribution for q_n in (A.4). In the last line of (A.4), the sin function can be written as $\frac{1}{2i}(e^{iqru} + e^{-iqru})$. The integration contour closes either on upper plane or lower plane depending on the position of the pole q_n considered. For example, in (a) the contour is for the term involving q_2. However at large distance only the two poles on the real axis contribute. And these are the only poles for the case of monolayer graphene $N = 1$ considered in this work, as is shown in (b). The principle values for these two terms are realized by the infinitesimal semi-circle contour and residue theorem.

where in the last line the integral definition of integer value Bessel function is used again. Notice the recursion relation of the Bessel functions

$$J_L(qr) = (-1)^L (qr)^L \left(\frac{1}{qr}\frac{\mathrm{d}}{\mathrm{d}(qr)}\right)^L J_0(qr). \tag{A.6}$$

$I^{(2)}_{L,M,N}(\boldsymbol{r},\omega)$ can be further written as

$$\begin{aligned} I^{(2)}_{L,M,N}(\boldsymbol{r},\omega) &= -\xi^L e^{iL\xi(\theta_{\boldsymbol{r}}+\frac{\pi}{2})}(-1)^L r^L \left(\frac{1}{r}\frac{\mathrm{d}}{\mathrm{d}r}\right)^L \int_0^\infty \frac{\mathrm{d}q}{2\pi}\frac{q^{2M+1}}{\omega^2 - q^{2N}} J_0(qr) \\ &= -\xi^L e^{iL\xi(\theta_{\boldsymbol{r}}+\frac{\pi}{2})}(-1)^L r^L \left(\frac{1}{r}\frac{\mathrm{d}}{\mathrm{d}r}\right)^L I^{(1)}_{M,N}(\boldsymbol{r},\omega). \end{aligned} \tag{A.7}$$

From (3.2), setting $v_F = 1$, the Green function for gapless graphene becomes

$$G^{(0)}(\boldsymbol{r},\boldsymbol{0};\omega) = \sum_\xi e^{i\boldsymbol{K}^\xi\cdot\boldsymbol{r}} \begin{pmatrix} \omega I^{(1)}_{0,1}(\boldsymbol{r},\omega) & \xi I^{(2)}_{1,0,1}(\boldsymbol{r},\omega) \\ \xi I^{(2)\prime}_{1,0,1}(\boldsymbol{r},\omega) & \omega I^{(1)}_{0,1}(\boldsymbol{r},\omega) \end{pmatrix}, \tag{A.8}$$

where $I^{(2)\prime}_{1,0,1}(\boldsymbol{r},\omega)$ is just $I^{(2)}_{1,0,1}(\boldsymbol{r},\omega)$ with $\theta_{\boldsymbol{r}}$ substituted by $-\theta_{\boldsymbol{r}}$. Thanks to the recursion relation (A.7), once $I_{0,1}(\boldsymbol{r},\omega)$ is calculated, it's done. From the last line of (A.4),

$$I^{(1)}_{0,1}(\boldsymbol{r},\omega) = \frac{1}{2\pi^2}\int_1^\infty \frac{\mathrm{d}u}{\sqrt{u^2-1}} \times \frac{1}{2}\left(\int_{-\infty}^\infty \frac{\sin(qru)}{\omega + i0^+ - q}\mathrm{d}q + \int_{-\infty}^\infty \frac{\sin(qru)}{-(\omega+i0^+) - q}\mathrm{d}q\right). \tag{A.9}$$

From the famous result[13]

$$\lim_{\eta\to 0^+}\int_{-\infty}^\infty \frac{f(x)}{x - x_0 \pm i\eta} = \text{p.v.}\int_{-\infty}^\infty \frac{f(x)}{x-x_0}\mathrm{d}x \mp \int_{-\infty}^{+\infty} i\pi\delta(x-x_0)f(x)\mathrm{d}x, \tag{A.10}$$

the first integral in the bracket in (A.9) can be evaluated as

$$\begin{aligned}
-\int_{-\infty}^{\infty}\frac{\sin(qru)}{q-\omega-i0^{+}}\mathrm{d}q &= -\left(\text{p.v.}\int_{-\infty}^{+\infty}\mathrm{d}q\frac{\sin(qru)}{q-\omega}+i\pi\int_{-\infty}^{\infty}\mathrm{d}q\delta(q-\omega)\sin(qru)\right)\\
&= -\left(\mathrm{Im}\int_{-\infty}^{\infty}\frac{e^{iqr}}{q-\omega}\mathrm{d}q+i\pi\sin(\omega ru)\right)\\
&= -\left(\pi\cos(\omega ru)+i\pi\sin(\omega ru)\right).
\end{aligned} \tag{A.11}$$

In the last line, the residue theorem is used to compute the principle value. For the second integral in bracket in (A.9), the same result is obtained following the same procedure. Thus $I^{(1)}_{0,1}(\boldsymbol{r},\omega)$ is finally calculated as

$$I^{(1)}_{0,1}(\boldsymbol{r},\omega) = -\frac{1}{2\pi}\int_{1}^{\infty}\frac{e^{i\omega ru}}{\sqrt{u^2-1}}\mathrm{d}u = -\frac{i}{4}H^{(1)}_{0}(\omega r). \tag{A.12}$$

From the recursion relation and (A.8), the real space, the real space Green function for gapless graphpene is finally obtained as

$$G^{(0)}(\boldsymbol{r},\boldsymbol{0};\omega) = \sum_{\xi}e^{i\boldsymbol{K}^{\xi}\cdot\boldsymbol{r}}\begin{pmatrix}-\frac{i\omega}{4}H^{(1)}_{0}(\omega r) & -\frac{\omega}{4}\xi e^{i\xi\theta_{\boldsymbol{r}}}H_1(\omega r)\\ -\frac{\omega}{4}\xi e^{-i\xi\theta_{\boldsymbol{r}}}H_1(\omega r) & -\frac{i\omega}{4}H^{(1)}_{0}(\omega r)\end{pmatrix}. \tag{A.13}$$

Restoring the v_F will just give (3.3) in the main text.

For gapped graphene, the integral expression of the Green function, compared to (3.2), becomes

$$G^{(0)}(\boldsymbol{r},\boldsymbol{0};\omega) = \sum_{\xi}e^{i\boldsymbol{K}^{\xi}\cdot\boldsymbol{r}}\int_{\mathbb{R}^2}\frac{\mathrm{d}q^2}{(2\pi)^2}\frac{e^{i\boldsymbol{q}\cdot\boldsymbol{r}}}{\omega^2-M^2-q^2}\begin{pmatrix}\omega+M & \xi q e^{i\xi\theta_{\boldsymbol{q}}}\\ \xi q e^{-i\xi\theta_{\boldsymbol{q}}} & \omega-M\end{pmatrix}. \tag{A.14}$$

If $|\omega|>M$, i.e., in the energy range outside the band gap, the procedure is the same as above, with the role of ω replaced by $\Omega\equiv\sqrt{\omega^2-M^2}$. The Green function for gapped graphene in this energy range is

$$G^{(0)}(\boldsymbol{r},\boldsymbol{0};\omega) = \sum_{\xi}\frac{e^{i\boldsymbol{K}^{\xi}\cdot\boldsymbol{r}}}{4v_F^2}\begin{pmatrix}-i(\omega+M)H^{(1)}_{0}(\frac{\Omega r}{v_F}) & \Omega\xi e^{i\xi\theta_{\boldsymbol{r}}}H^{(1)}_{1}(\frac{\Omega r}{v_F})\\ \Omega\xi e^{-i\xi\theta_{\boldsymbol{r}}}H^{(1)}_{1}(\frac{\Omega r}{v_F}) & -i(\omega-M)H^{(1)}_{0}(\frac{\Omega r}{v_F})\end{pmatrix}. \tag{A.15}$$

The LDOS modulation calculated from (A.15) will still display the Friedel oscillation.

However, inside the gap $\omega\in(-M,M)$, the calculation is performed with a slight difference. This time define $\Omega\equiv\sqrt{M^2-\omega^2}\in(0,M)$. Then the integral $I^{(1)}_{M,N}$ becomes

$$\begin{aligned}
I^{(1)}_{M,N}(\boldsymbol{r},i\Omega) &= \int_{\mathbb{R}}\frac{\mathrm{d}q^2}{(2\pi)^2}\frac{q^{2M}}{-\Omega^2-q^{2N}}e^{i\boldsymbol{q}\cdot\boldsymbol{r}}\\
&= -\frac{1}{2\pi^2}\int_{1}^{\infty}\frac{\mathrm{d}u}{\sqrt{u^2-1}}\int_{-\infty}^{\infty}\frac{q^{2M+1}\sin(qru)}{\Omega^2+q^{2N}}\mathrm{d}q\\
&= -\frac{1}{2\pi^2}\int_{1}^{\infty}\frac{\mathrm{d}u}{\sqrt{u^2-1}}\sum_{n=0}^{2N-1}\frac{1}{2Nq_n^{2(N-M-1)}}\int_{\mathbb{R}}\mathrm{d}q\frac{\sin(qru)}{q-q_n}.
\end{aligned} \tag{A.16}$$

The same steps in (A.4) are also performed here and the result looks the same. The difference is in the distribution of poles. Now $q_n = \Omega^{1/N} e^{i\frac{2n+1}{2N}\pi}$. There are no more poles on the real axis. This is shown in Fig 14.

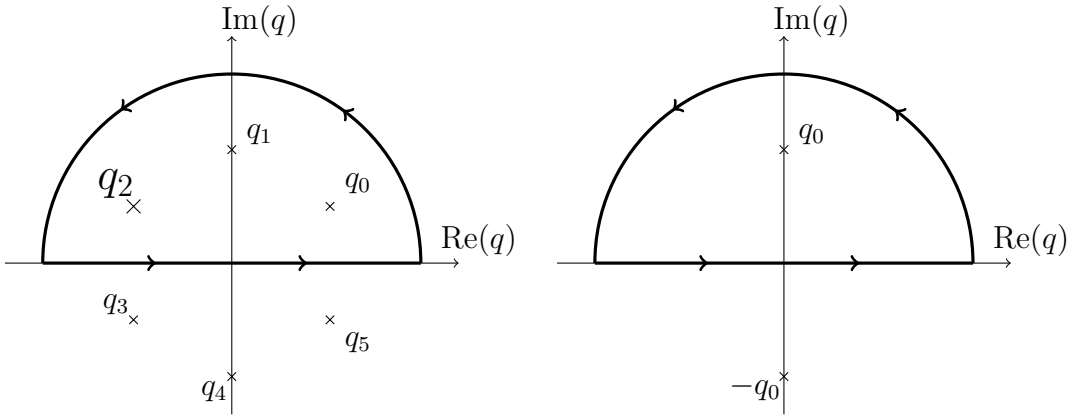

(a) $N = 3$ for gapped graphene (b) $N = 1$ for gapped graphene

Figure 14: A sketch for $q_n = \Omega^{1/N} e^{i\frac{2n+1}{2N}\pi}$ in (A.16). Again, the contour giving non-zero contribution closes according to the position of the pole. There are no more poles on the real axis. This is the cause of exponential decay for charged density oscillation in the band gap.

For one pole labelled from 0 to $2N-1$ in the summation, the integral can be written as

$$\int_{\mathbb{R}} \mathrm{d}q \frac{\sin(qru)}{q - q_n} = \frac{1}{2i} \int_{-\infty}^{\infty} \mathrm{d}q \frac{e^{iqru} - e^{-iqru}}{q - q_n}. \tag{A.17}$$

Notice that $ru > 0$, the integration contour will close on the upper complex plane for the first term and on lower complex plane for the second term. Depending on the position of pole considered, only one term will contribute to this integral. Integrate it out for each term in the summation,

$$I^{(1)}_{MN}(\boldsymbol{r}, \omega = i\Omega) = -\frac{1}{2\pi^2} \int_1^{+\infty} \frac{du}{\sqrt{u^2-1}} \sum_{n=0}^{2N-1} \pi \frac{\exp\left[i \cdot \mathrm{sgn}\left[\mathrm{Im}(q_n)\right] \cdot ru\Omega^{\frac{1}{N}} e^{i\frac{2n+1}{2N}\pi}\right]}{2N q_n^{2(N-M-1)}}. \tag{A.18}$$

In the case of monolayer graphene considered here, $N = 1$, thus

$$\begin{aligned} I^{(1)}_{0,1}(\boldsymbol{r}, i\Omega) &= -\frac{1}{2\pi^2} \int_1^{+\infty} \frac{du}{\sqrt{u^2-1}} \frac{\pi}{2} \left[\exp\left(iru\Omega e^{i\frac{\pi}{2}}\right) + \exp\left(-iru\Omega e^{i\frac{3\pi}{2}}\right)\right] \\ &= -\frac{1}{2\pi} \int_1^{+\infty} \frac{du}{\sqrt{u^2-1}} e^{-\Omega ru} = -\frac{1}{2\pi} K_0(\Omega r) \end{aligned}. \tag{A.19}$$

$K_0(x)$ is the zeroth order modified Bessel function of the second kind. Making use of the derivative recursion relation,

$$\begin{aligned} I^{(2)}_{1,0,1}(\boldsymbol{r}, i\Omega) &= -e^{i\xi\theta_{\boldsymbol{r}}}(-i)r\left(\frac{1}{r}\frac{\mathrm{d}}{\mathrm{d}r}\right) I^{(1)}_{0,1}(\boldsymbol{r}, i\Omega) \\ &= -\frac{i}{2\pi}e^{i\xi\theta_{\boldsymbol{r}}}\Omega\frac{\mathrm{d}}{\mathrm{d}(\Omega r)}K_0(\Omega r) \qquad . \\ &= \frac{i\Omega}{2\pi}e^{i\xi\theta_{\boldsymbol{r}}}K_1(\Omega r) \end{aligned} \tag{A.20}$$

Finally, the Green function for gapped graphene is obtained as

$$G^{(0)}(\boldsymbol{r}, \omega) = \sum_{\xi}\frac{e^{i\boldsymbol{K}^{\xi}\cdot\boldsymbol{r}}}{2\pi}\begin{pmatrix} -(\omega+M)K_0(\Omega r) & -i\xi\Omega e^{i\xi\theta_{\boldsymbol{r}}}K_1(\Omega r) \\ -i\xi\Omega e^{-i\xi\theta_{\boldsymbol{r}}}K_1(\Omega r) & -(\omega-M)K_0(\Omega r)\end{pmatrix}. \tag{A.21}$$

Restoring v_F will give (3.7) in the main text.

References

[1] D. C. Tsui, H. L. Stormer, and A. C. Gossard, "Two-dimensional magnetotransport in the extreme quantum limit," *Phys. Rev. Lett.*, vol. 48, pp. 1559–1562, May 1982.

[2] R. B. Laughlin, "Anomalous quantum hall effect: An incompressible quantum fluid with fractionally charged excitations," *Phys. Rev. Lett.*, vol. 50, pp. 1395–1398, May 1983.

[3] W. X. Gang, *Quantum field theory of many-body systems: from the origin of sound to an origin of light and electrons*. Oxford: Oxford University Press, 2007.

[4] X. G. Wen, "Topological Order in Rigid States," *Int. J. Mod. Phys. B*, vol. 4, p. 239, 1990.

[5] M. V. Berry, "Quantal phase factors accompanying adiabatic changes," *Proc. R. Soc. Lond. A*, vol. 392, pp. 45–57, March 1984.

[6] P. Mallet, I. Brihuega, S. Bose, M. M. Ugeda, J. M. Gómez-Rodríguez, K. Kern, and J. Y. Veuillen, "Role of pseudospin in quasiparticle interferences in epitaxial graphene probed by high-resolution scanning tunneling microscopy," *Phys. Rev. B*, vol. 86, p. 045444, Jul 2012.

[7] K. S. Novoselov, A. K. Geim, S. V. Morozov, D. Jiang, M. I. Katsnelson, I. V. Grigorieva, S. V. Dubonos, and A. A. Firsov, "Two-dimensional gas of massless dirac fermions in graphene," *Nature*, vol. 438, pp. 197–200, Nov. 2005.

[8] C. Dutreix, H. González-Herrero, I. Brihuega, M. I. Katsnelson, C. Chapelier, and V. Renard, "Measuring the Berry phase of graphene from wavefront dislocations in Friedel oscillations," *Nature*, vol. 574, pp. 219–222, Sept. 2019.

[9] C. Dutreix and M. I. Katsnelson, "Friedel oscillations at the surfaces of rhombohedral n-layer graphene," *Phys. Rev. B*, vol. 93, p. 035413, Jan 2016.

[10] C. Bena, "Effect of a single localized impurity on the local density of states in monolayer and bilayer graphene," *Phys. Rev. Lett.*, vol. 100, p. 076601, Feb 2008.

[11] C. Dutreix and P. Delplace, "Geometrical phase shift in friedel oscillations," *Phys. Rev. B*, vol. 96, p. 195207, Nov 2017.

[12] J. F. Nye and M. V. Berry, "Dislocations in Wave Trains," *Proceedings of the Royal Society of London Series A*, vol. 336, pp. 165–190, Jan. 1974.

[13] E. Saff, A. Snider, L. Trefethen, and T. Driscoll, *Fundamentals of Complex Analysis with Applications to Engineering and Science*. Prentice Hall, 2003.